CHAPTER – 6

Corrosion and biocompatibility of the Ti-Zr-Nb-Mo-Fe-Cr based bio-CCA

6.1 Background

Metallic implant biomaterials are widely used to support, replace, or repair damaged tissues and organs in the human body. However, it is well established that the physiological environment within the body is chemically and physically distinct from ambient conditions, presenting a harsh and aggressive setting for metallic implants [9]. Consequently, alloys that remain inert or passive in air may undergo significant corrosion when exposed to a physiological environment. Even localized corrosion of an implanted device can lead to premature failure and increased release of metallic ions into surrounding tissues, potentially affecting both local and overall biological functions [208].

Additionally, orthopedic implant materials should be functionalized to mimic the properties of natural bone, thereby enhancing integration and accelerating bone regeneration. In the case of bioactive materials, a bone-like apatite layer can spontaneously form on the implant surface, promoting strong bone bonding and supporting both osseointegration and osteogenesis [209]. Therefore, to achieve effective integration with the surrounding bone, it is crucial for an implant to possess an appropriately engineered surface. The key surface parameters that must be carefully considered for good osseointegration include surface chemistry, roughness, wettability, and topography [9,210-212].

Based on the aforementioned background, this chapter aims to investigate the corrosion and biocompatibility behaviour of the $Ti_{35}Zr_{35}Nb_{15}Mo_5Fe_5Cr_5$ bio-CCA, and to compare the results with those of 316L stainless steel (SS) and cp-Ti. The results presented in this chapter are divided into four sections. The first two sections focus on the electrochemical corrosion behaviour of the present bio-CCA in simulated body fluid (SBF) solution, using potentiodynamic polarization and electrochemical impedance spectroscopy

(EIS). The third section provides a quantitative analysis of the cell culture study, including cell viability and proliferation, using MG-63 and HEK-293 cell lines. Finally, the fourth section qualitatively assesses MG-63 cell adhesion via confocal microscopy using various fluorescent dyes, including AO/EtBr, Rh-123, DAPI, and DCFH-DA.

6.2 Results

6.2.1 Potentiodynamic polarization of $Ti_{35}Zr_{35}Nb_{15}Mo_5Fe_5Cr_5$ bio-CCA

The electrochemical corrosion behaviour of the as-cast and annealed bio-CCA was studied in SBF solution. The potentiodynamic polarization curves of the as-cast and annealed $Ti_{35}Zr_{35}Nb_{15}Mo_5Fe_5Cr_5$ bio-CCA, cp-Ti, and 316L SS are shown in Figure 6.1. The electrochemical parameters, such as corrosion potential (V_{corr}) and corrosion current density (I_{corr}), were determined by extrapolating the potentiodynamic polarization curves, with the corresponding values summarized in Table 6.1. The results indicate that both the as-cast and annealed CCA specimens exhibit higher corrosion potentials than cp-Ti and 316L SS. Notably, the corrosion potential of the annealed CCA increases progressively with increasing annealing temperatures. According to chemical thermodynamics, a higher corrosion potential corresponds to enhanced corrosion resistance. Among all the samples, the specimen annealed at 1100°C demonstrates the highest corrosion potential of 6.93 mV, indicating superior corrosion resistance.

Although the corrosion rate of alloys is determined from the corrosion current density (using Equation 3.15), it is crucial to understand that corrosion resistance is inversely related to both I_{corr} and the corrosion rate. The I_{corr} of the as-cast CCA is slightly lower than that of cp-Ti, and significantly lower than that of 316L SS, suggesting that the corrosion rate of the

as-cast CCA is considerably lower compared to 316L SS. As presented in Table 6.1, the I_{corr} value for the annealed CCA is notably lower than the as-cast state, signifying an enhancement in corrosion resistance upon annealing. Specifically, the I_{corr} values for the as-cast CCA, 1100°C annealed CCA, cp-Ti, and 316L SS are 0.79 µA/cm², 0.2084 µA/cm², 0.8194 µA/cm², and 7.564 µA/cm², respectively. These findings demonstrate that the corrosion resistance of the bio-CCA is superior to both cp-Ti and 316L SS in SBF solution.

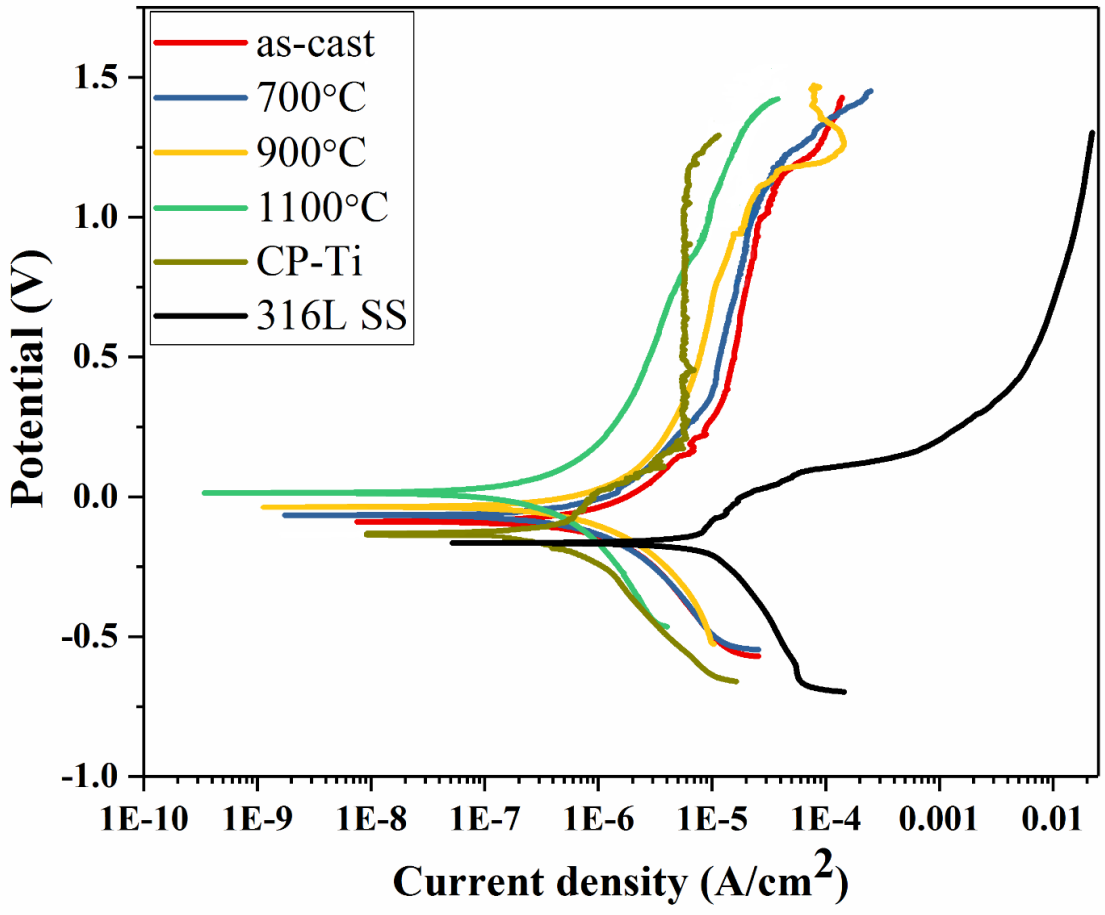

Figure 6.1 Potentiodynamic polarization curve of the $Ti_{35}Zr_{35}Nb_{15}Mo_5Fe_5Cr_5$ CCA, cp-Ti, and 316L SS in SBF solution.

Table 6.1: Electrochemical parameters of the as-cast and annealed $Ti_{35}Zr_{35}Nb_{15}Mo_5Fe_5Cr_5$ CCA, cp-Ti, and 316L SS in the SBF solution.

CCA	Corrosion potential (V_{corr})	Corrosion current density (A/cm^{-2})	Corrosion rate (mm/year)
$Ti_{35}Zr_{35}Nb_{15}Mo_5Fe_5Cr_5$ (as-cast)	-0.0836	7.907×10^{-7}	7.43×10^{-3}
$Ti_{35}Zr_{35}Nb_{15}Mo_5Fe_5Cr_5$ (700ºC)	-0.0652	7.394×10^{-7}	6.94×10^{-3}
$Ti_{35}Zr_{35}Nb_{15}Mo_5Fe_5Cr_5$ (900ºC)	-0.0411	5.046×10^{-7}	4.74×10^{-3}
$Ti_{35}Zr_{35}Nb_{15}Mo_5Fe_5Cr_5$ (1100ºC)	0.00693	2.084×10^{-7}	1.95×10^{-3}
cp-Ti	-0.1352	8.194×10^{-7}	7.13×10^{-3}
316L SS	-0.1611	7.654×10^{-6}	88.19×10^{-3}

Figure 6.2 exhibits the SEM surface morphology of the $Ti_{35}Zr_{35}Nb_{15}Mo_5Fe_5Cr_5$ CCA in both as-cast and annealed states after potentiodynamic polarization testing in SBF. As shown in Figure 6.2 (a), the corroded surface of the as-cast alloy exhibits localized corrosion characterized by numerous pits, indicating that pitting is the dominant corrosion mechanism in the as-cast state. In contrast, Figures 6.2 (b–d) reveal a noticeable reduction in both pit size and pit number density with increasing annealing temperature. Notably, the surface of the alloy annealed at 1100°C appears significantly smoother, with fewer and smaller pits,

suggesting that annealing improves the alloy's resistance to pitting corrosion. EDS analysis of the corroded surface (Figure 6.3 a–b) reveals that the CCA annealed at 1100°C contains a significantly higher oxygen content than the as-cast alloy. This higher oxygen concentration contributes to forming a thicker oxide layer on the surface, which acts as a protective barrier against anodic corrosion, thereby improving the corrosion resistance of the annealed CCA.

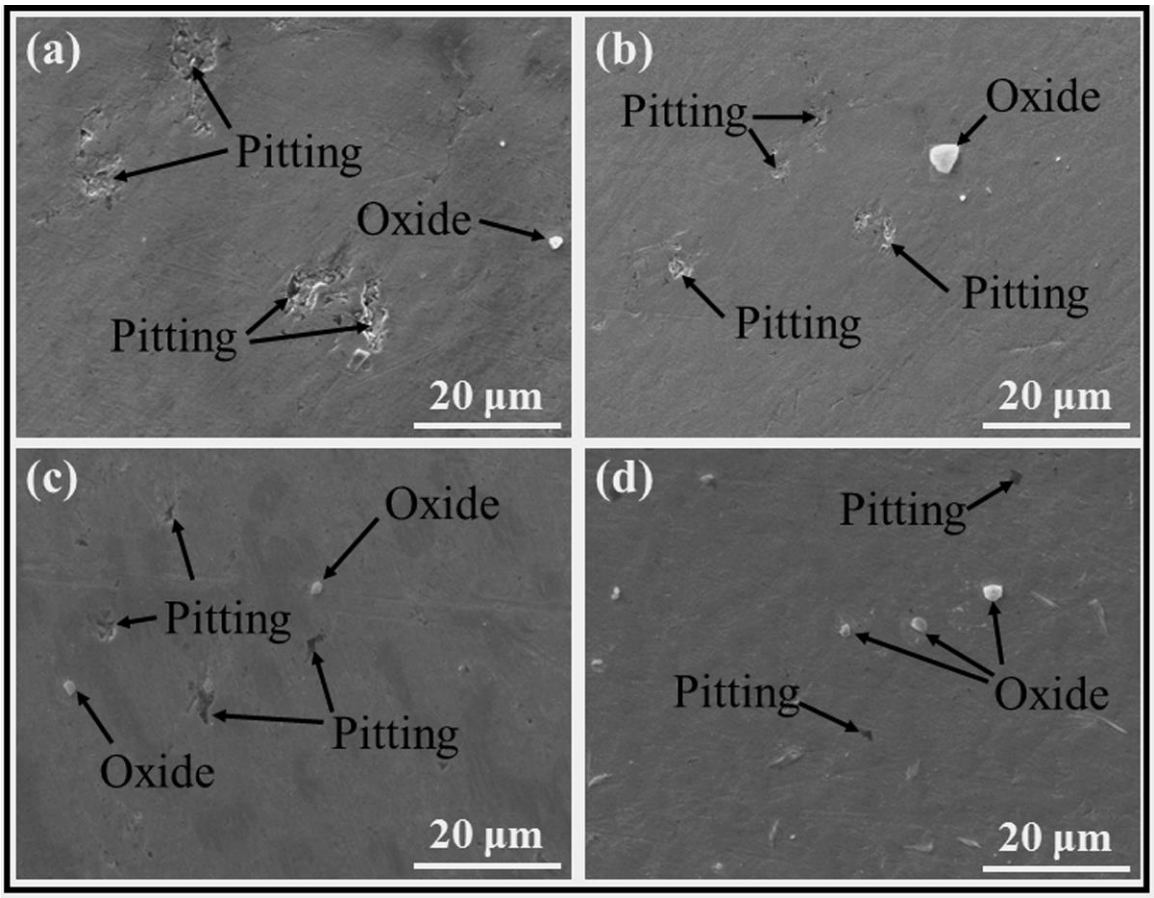

Figure 6.2 SEM image of the corroded surface of the $Ti_{35}Zr_{35}Nb_{15}Mo_5Fe_5Cr_5$ CCA (a) as-cast, (b) 700˚C, (c) 900˚C, and (d) 1100˚C annealed alloy in SBF solution.

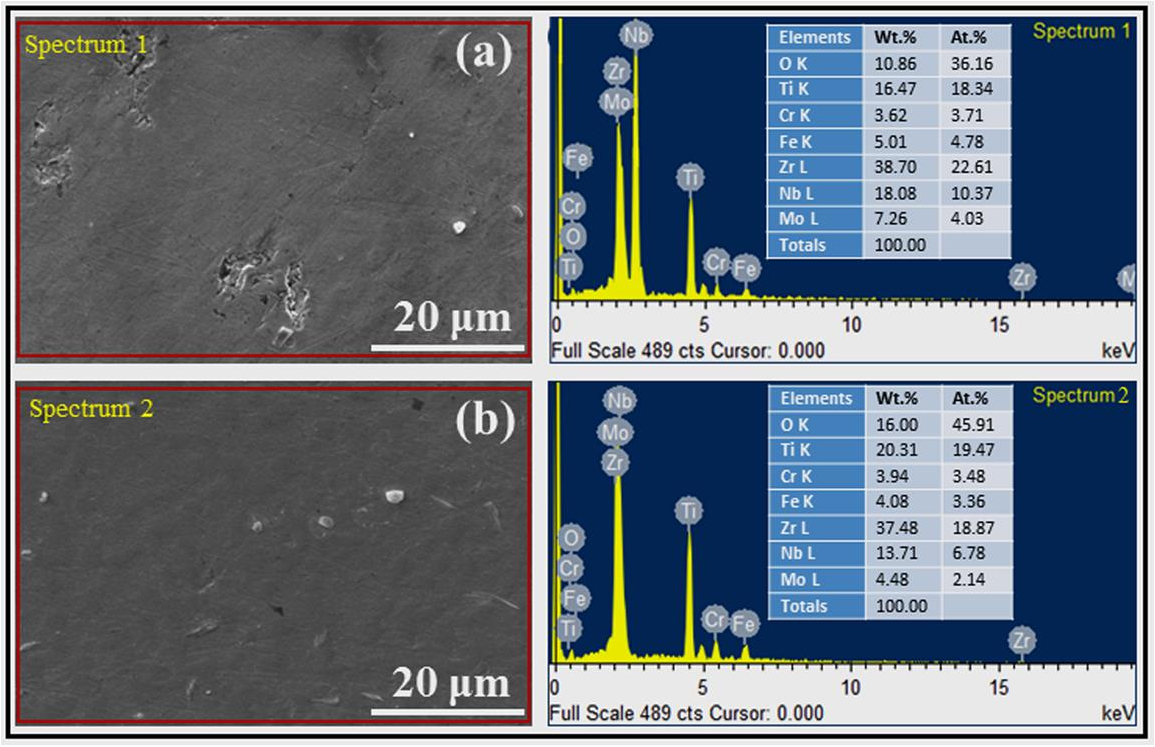

Figure 6.3 EDS area spectrum of the $Ti_{35}Zr_{35}Nb_{15}Mo_5Fe_5Cr_5$ CCA after potentiodynamic polarization experiment (a) as-cast, and (b) 1100˚C annealed condition.

6.2.2 Electrochemical impedance spectroscopy analysis of $Ti_{35}Zr_{35}Nb_{15}Mo_5Fe_5Cr_5$ bio-CCA

Electrochemical impedance spectroscopy (EIS) was conducted on all samples to investigate their passivation behavior. The EIS results, obtained after one hour of immersion in SBF solution, are presented as Nyquist and Bode plots (Figure 6.4). In the Nyquist plots, which depict the imaginary versus real components of impedance, all samples exhibit characteristic semicircular arcs. The diameter of these arcs corresponds to the polarization resistance of the passive films. As shown in Figure 6.4(a), the as-cast $Ti_{35}Zr_{35}Nb_{15}Mo_5Fe_5Cr_5$ CCA displays a larger semicircular arc compared to 316L SS and cp-Ti, indicating that the passive film formed on the CCA has superior resistance and, consequently, provides better

protection. Additionally, with increasing annealing temperature, the radius of the Nyquist semicircular arc progressively increases, and the CCA annealed at 1100°C exhibits the largest arc radius. This indicates that the CCA annealed at 1100°C possesses significantly enhanced corrosion resistance in the SBF solution compared to the other samples (i.e., as-cast CCA, cp-Ti, and 316L SS).

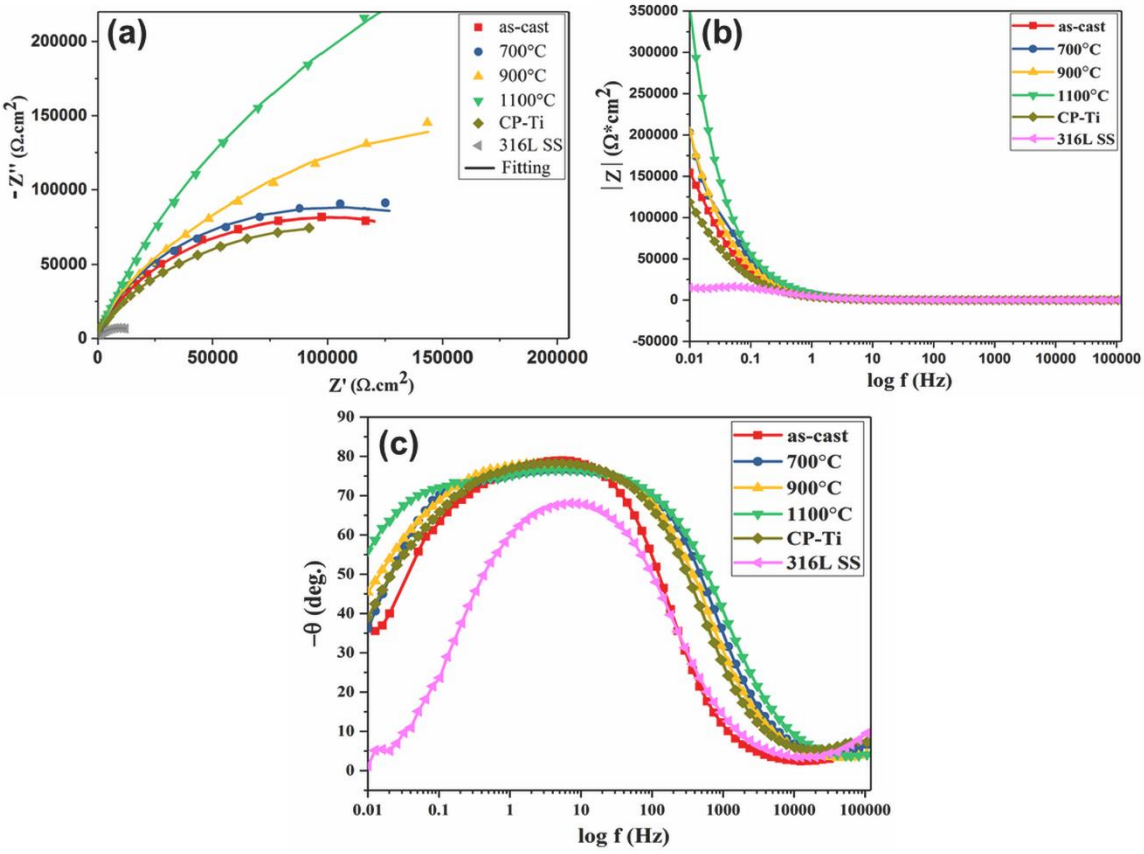

Figure 6.4 EIS spectra of the $Ti_{35}Zr_{35}Nb_{15}Mo_5Fe_5Cr_5$ CCA, cp-Ti, and 316L SS in SBF solution (a) Nyquist plot and (b, c) Bode plots.

In the Bode plot (Figure 6.4 (b and c)), the impedance modulus remains relatively constant across all samples, while the phase angle approaches zero degrees in the high-frequency region, indicating resistor-like behaviour. This response is attributed to the

dominance of solution resistance at higher frequencies [208]. In contrast, at medium to low frequencies, the Bode plots for both the as-cast and annealed CCA samples, as well as cp-Ti, show phase angles nearing −80°, indicating highly capacitive behaviour and the presence of a robust oxide layer on the surface in the SBF solution. Conversely, for 316L SS, the phase angle in the mid-frequency range approaches −65°, suggesting that the oxide layer formed on its surface is weaker compared to that on the CCA samples and cp-Ti.

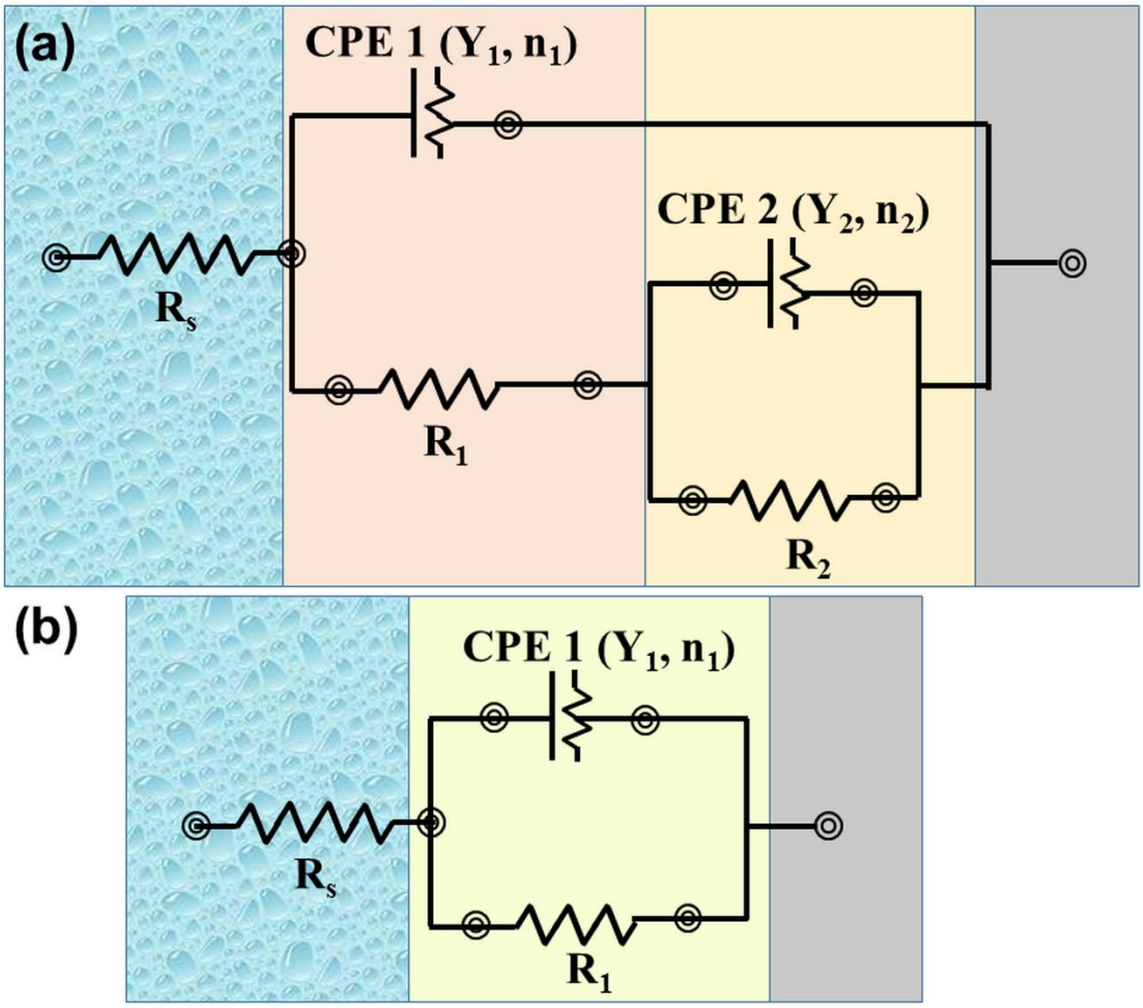

Figure 6.5 Equivalent electrical circuit (EEC) used to fit the data (a) EEC for CCA and cp-Ti, and (b) for 316L SS.

The ZView® software was utilized to analyze the impedance characteristics using equivalent electrical circuits (EECs), as illustrated in Figure 6.5 (a) and (b). For the CCA and cp-Ti, the EEC model shown in Figure 6.5 (a) includes components R_S, R_1, and R_2, which correspond to the resistance of the SBF solution, the outer porous layer, and the inner barrier layer, respectively. CPE1 and CPE2 represent the constant phase elements associated with the outer porous layer and inner barrier layers. In contrast, the EEC for 316L SS, shown in Figure 6.5 (b), consists of R_S, R_1, and a CPE_1. The impedance parameters obtained by fitting the EIS data to these circuits are summarized in Table 6.2. The standard deviation parameter (χ^2) for both proposed circuits is on the order of 10^{-3} or lower, indicating a good fit between the experimental data and the proposed circuit models, in accordance with established fitting criteria [213].

Table 6.2: Impedance parameters of the suggested EEC elements are achieved by fitting them with the EIS experimental results of $Ti_{35}Zr_{35}Nb_{15}Mo_5Fe_5Cr_5$ CCA, cp-Ti, and 316L SS in SBF solution.

CCA	R_s (Ω cm^2)	R_1 (kΩ cm^2)	CPE 1		R_2 (kΩ cm^2)	CPE 2		χ^2*10^{-3}
			Y_1*10^{-5} (Ω^{-1} $cm^{-2}s^{n1}$)	n_1		Y_2*10^{-5} (Ω^{-1} $cm^{-2}s^{n2}$)	n_2	
$Ti_{35}Zr_{35}Nb_{15}Mo_5Fe_5Cr_5$ (as-cast)	23.05	108.12	12.92	0.89	155.92	9.18	0.91	0.367

$Ti_{35}Zr_{35}Nb_{15}Mo_5Fe_5Cr_5$ (700ºC annealed)	21.24	124.03	10.67	0.90	180.41	2.52	0.94	0.951
$Ti_{35}Zr_{35}Nb_{15}Mo_5Fe_5Cr_5$ (900ºC annealed)	19.46	132.60	6.43	0.87	216.89	3.03	0.92	3.924
$Ti_{35}Zr_{35}Nb_{15}Mo_5Fe_5Cr_5$ (1100ºC annealed)	20.04	339.36	2.44	0.85	569.73	5.06	0.93	2.173
cp-Ti	18.88	85.89	9.811	0.86	96.31	4.601	0.88	1.632
316L SS	26.78	16.80	8.269	0.81	-	-	-	4.013

The impedance of the constant phase element (CPE) is mathematically represented as:

$$Z_{CPE} = [Y_0(j\omega)^n]^{-1} \quad \text{..... (6.1)}$$

In this expression, n is the CPE exponent that reflects the degree of surface heterogeneity and ranges between −1 and 1. Y_0 denotes the proportionality constant, while j and ω represent the imaginary unit and angular frequency, respectively [67]. The exponent n is influenced by surface imperfections and irregularities, which lead to a non-uniform distribution of current. When n approaches 1, the CPE behaves similarly to an ideal capacitor. Based on the proposed equivalent electrical circuit, the capacitance value of CPE2, representing the inner barrier layer, is lower than that of CPE1, which corresponds to the outer porous layer, across both as-cast and annealed CCA samples. A lower capacitance typically indicates a thicker protective layer and a lower dielectric constant of the oxide film, which may result from

variations in the volume ratio between the electrolyte solution and the oxide layer [174-175]. In the present study, the combination of lower CPE2 and higher R_2 values observed for both the as-cast and annealed CCA and cp-Ti indicates that the inner barrier layer plays a dominant role in providing corrosion resistance.

6.2.3 Contact angle measurement

Contact angle measurements were performed on as-cast and annealed CCA specimens, cp-Ti, and 316L SS under controlled conditions of 40% relative humidity and a temperature of 20 °C. The result of contact angle measurements is presented in Figure 6.6. Droplet profiles were analyzed using the ellipse fitting method, with five measurements taken for each sample. The as-cast and 1100°C annealed CCA specimens exhibited average contact angles of $59.8° \pm 2.4°$ and $55.1° \pm 1.5°$, respectively. In comparison, the 316L stainless steel and cp-Ti samples showed higher average contact angles of $75.5° \pm 2.9°$ and $70.5° \pm 1.8°$, respectively.

Contact angle measurements were used to evaluate the surface characteristics, specifically to determine whether the surfaces were hydrophilic or hydrophobic. A contact angle less than 90° indicates a hydrophilic surface, whereas a contact angle greater than 90° corresponds to a hydrophobic surface. In the present study, all samples exhibited contact angles below 90°, confirming their hydrophilic nature. Notably, the CCA samples showed lower contact angles compared to cp-Ti and 316L stainless steel, indicating a higher degree of hydrophilicity and improved surface wettability.

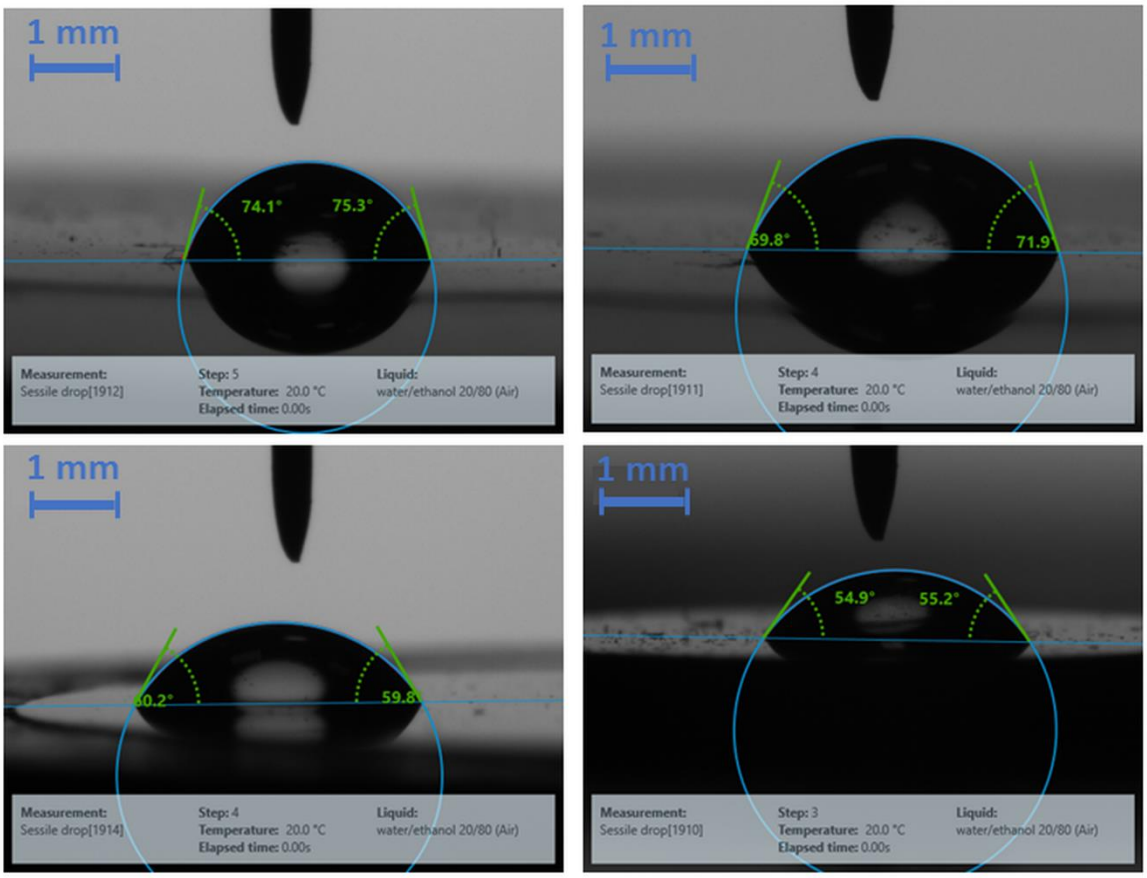

Figure 6.6 Contact angle measurement (a) 316 L SS, (b) cp-Ti, (c) as-cast CCA, and (d) 1100˚C annealed CCA.

6.2.4 In-vitro cytocompatibility evaluation of the $Ti_{35}Zr_{35}Nb_{15}Mo_5Fe_5Cr_5$ bio-CCA

Biocompatibility was evaluated for both the as-cast CCA and 1100°C annealed CCA, with the latter selected (among the various annealing conditions) due to its superior mechanical properties and highest resistance to corrosion and wear. To evaluate in-vitro cytocompatibility, the proliferation and viability of MG-63 and HEK-293 cells were analyzed and compared with conventional biomaterials, namely 316L SS and cp-Ti. The results of the MTT assay, conducted after 3 and 7 days of incubation, are shown in Figure 6.7. The

absorbance, which reflects the number of viable cells, gradually increases from day 3 to day 7, confirming continuous cell proliferation.

The CCA specimens show significantly higher absorbance (Figure 6.7 (a and b) than both 316L SS and cp-Ti, indicating enhanced cell viability. These findings are consistent with those reported by Nagase et al., who concluded that cell viability is strongly dependent on alloy composition [68]. Notably, the 1100°C annealed CCA exhibited the highest absorbance, suggesting that annealing further improves cell viability. This improvement is likely due to the redistribution of constituent elements and the resulting microstructural homogeneity achieved through annealing treatment [40].

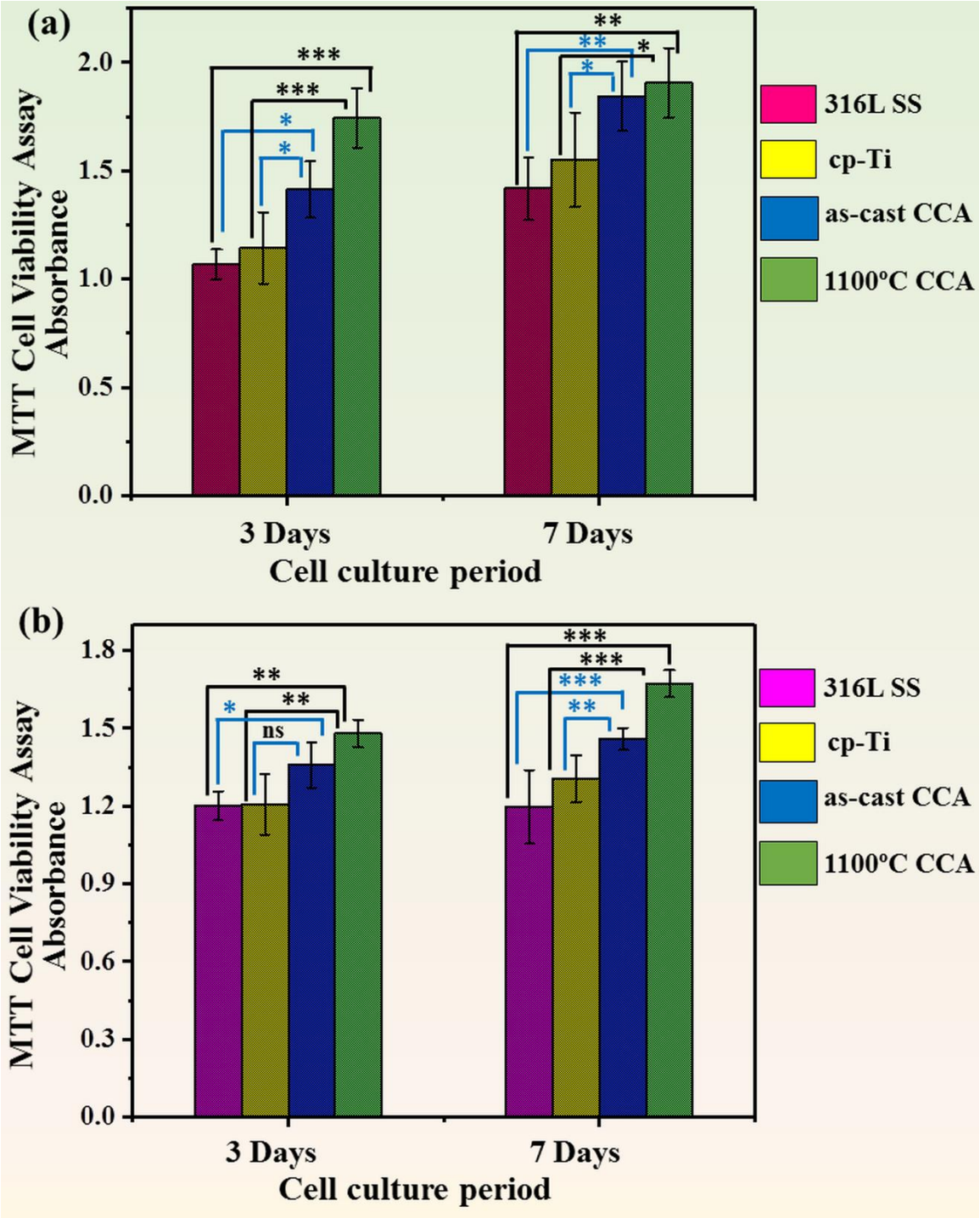

Figure 6.7 MTT assay findings for (a) MG-63 and (b) HEK-293 cell viability and proliferation activities after 3 and 7 days of incubation for the as-cast and 1100˚C annealed CCA, cp-Ti, and 316L SS. The results were expressed as mean ± standard deviation, and statistical significance was determined by comparing them to the control group (cp-Ti and 316L SS). Significance levels were denoted as: *p < 0.05, **p < 0.01, and ***p < 0.001.

The morphology of MG-63 cells adhered to the surfaces of the as-cast and 1100°C annealed CCA, CP-Ti, and 316L SS was evaluated using Acridine Orange/Ethidium Bromide (AO/EtBr) staining. As shown in Figure 6.8, confocal microscopy images reveal a higher number of green-fluorescing (live) cells on both the as-cast and 1100°C annealed CCA surfaces compared to 316L SS and CP-Ti. In addition, no significant presence of apoptotic (unhealthy or dead) cells was observed on the CCA samples.

In the present study, AO/EtBr staining was also used to evaluate the nuclear morphology of MG-63 cells. Acridine orange (AO) stains both viable and non-viable cells, whereas ethidium bromide (EtBr) selectively stains cells with compromised membrane integrity, a characteristic feature of apoptosis [214]. These staining properties allow for clear differentiation between apoptotic cells and those in the control samples (316L SS and cp-Ti). The results demonstrate that the $Ti_{35}Zr_{35}Nb_{15}Mo_5Fe_5Cr_5$ CCA does not induce apoptosis. Overall, the findings suggest that both the as-cast and 1100°C annealed CCA specimens exhibit superior cytocompatibility compared to 316L SS and cp-Ti.

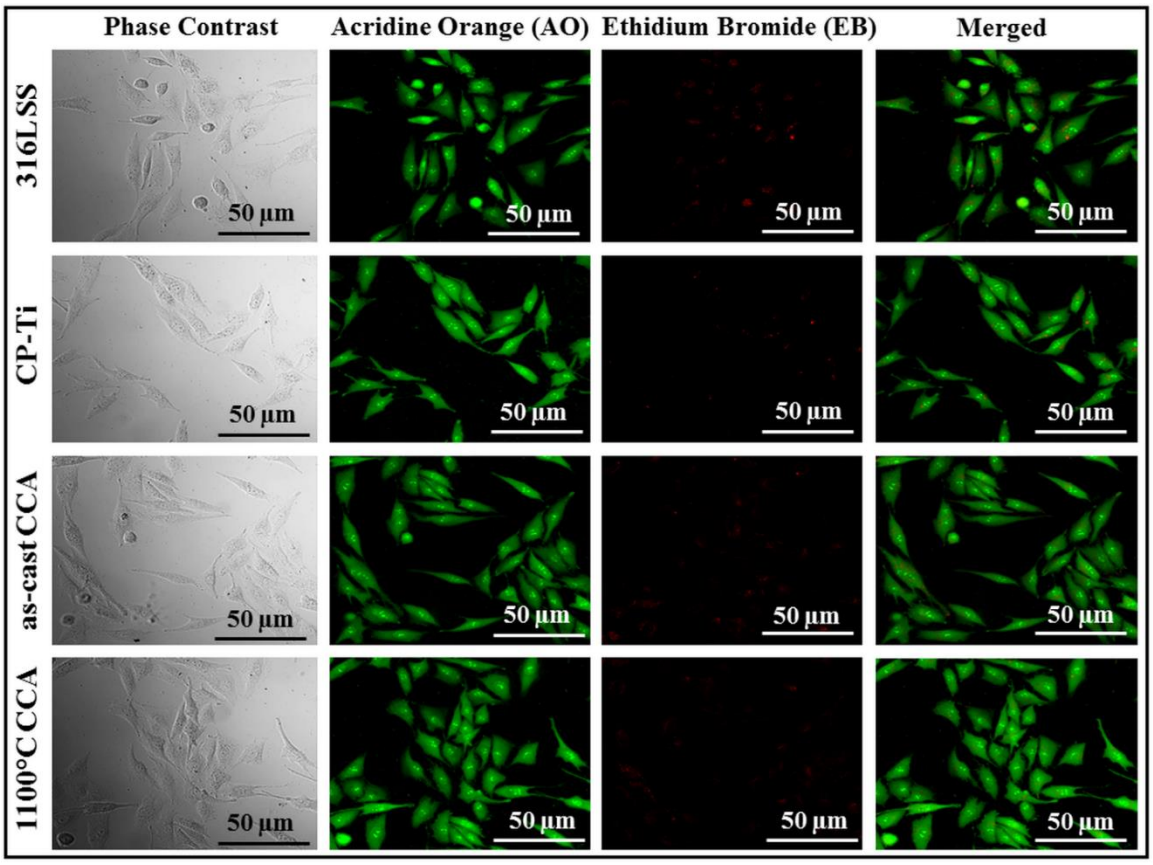

Figure 6.8 Confocal microscopy images of MG-63 cells adhered to the surface of as-cast and 1100˚C annealed CCA, cp-Ti, and 316L SS after 3 days of incubation and stained with AO/EtBr.

To evaluate nuclear morphological changes associated with apoptosis or necrosis in MG-63 cells, DAPI (4′,6-diamidino-2-phenylindole) staining was utilized [215]. DAPI binds strongly to adenine-thymine (A-T) rich regions of DNA due to its structural and chemical affinity, resulting in intense fluorescence upon binding. As shown in Figure 6.9, after three days of incubation with both the as-cast and 1100°C annealed CCA specimens, MG-63 cells largely retained their nuclear morphology. The nuclei appeared uniformly stained, smooth in appearance, and exhibited minimal DAPI-positive stains. In contrast, cells treated with 316L SS and cp-Ti exhibited notable morphological alterations, including nuclear fragmentation, chromatin condensation, and an increased number of DAPI-positive cells. These results suggest that the $Ti_{35}Zr_{35}Nb_{15}Mo_5Fe_5Cr_5$ CCA induces significantly less DNA or chromosomal damage compared to cp-Ti and 316L SS.

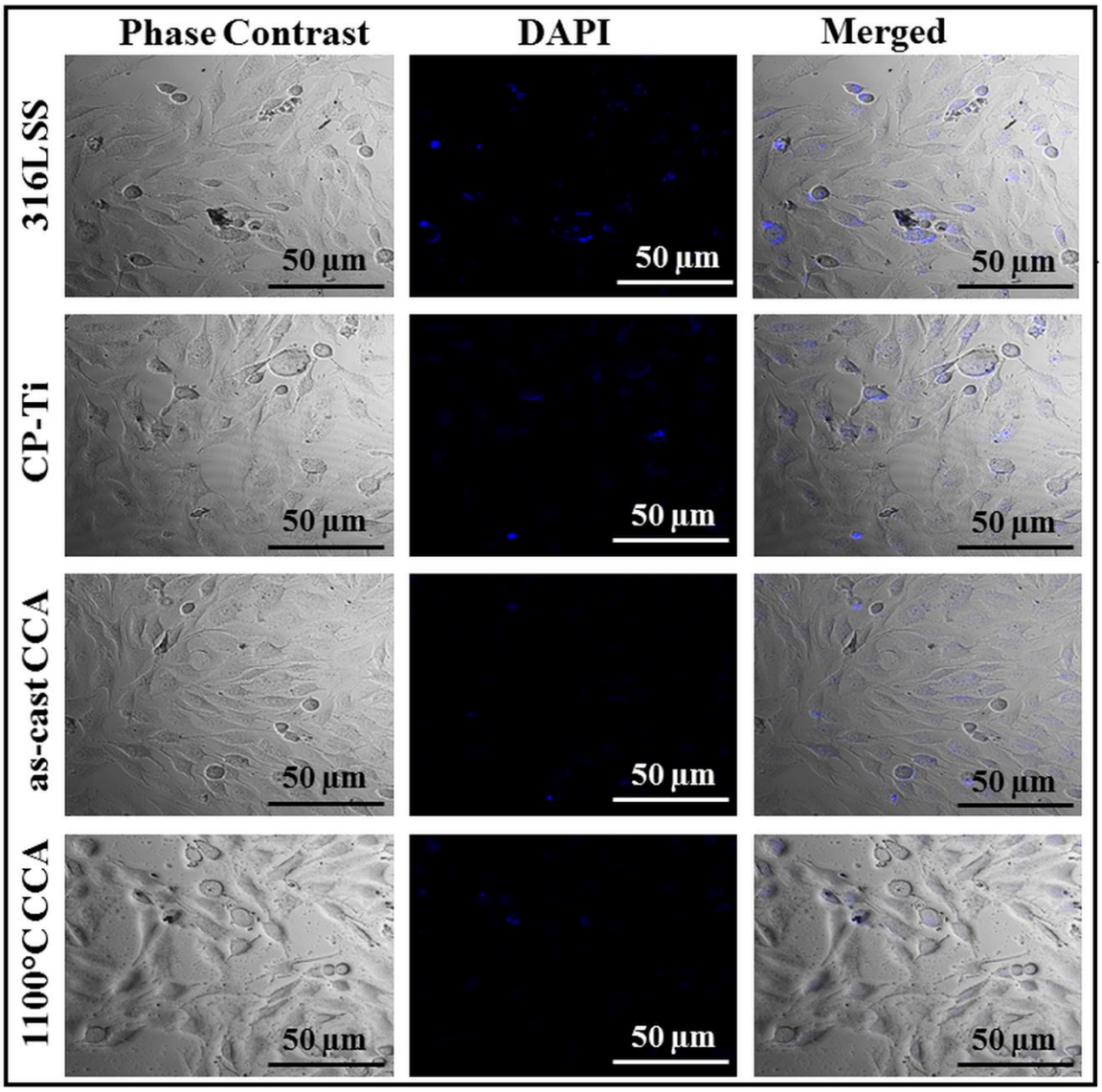

Figure 6.9 Nuclear morphology of the MG-63 cell on the surface of as-cast and 1100˚C annealed CCA, cp-Ti, and 316L SS using confocal microscopy with DAPI staining.

In addition, the cytocompatibility of the $Ti_{35}Zr_{35}Nb_{15}Mo_5Fe_5Cr_5$ CCA was assessed based on mitochondrial membrane potential using rhodamine-123 staining. This fluorescent dye selectively accumulates in active mitochondria, allowing the evaluation of concentration-dependent changes in mitochondrial membrane potential ($\Delta\Psi_m$). After three days of incubation, MG-63 cells were stained with rhodamine-123, which specifically targets the mitochondria of viable cells. Compared to 316L SS and cp-Ti, cells treated with both the as-

cast and 1100°C annealed CCA exhibited an increased $\Delta\Psi_m$. Confocal microscopy further confirmed these observations, revealing increased rhodamine-123 fluorescence intensity in the CCA-treated cells compared to 316L SS and cp-Ti (Figure 6.10). These results suggest that the as-cast and 1100°C annealed CCA enhances cytocompatibility with MG-63 cells, potentially through a mitochondria-dependent mechanism.

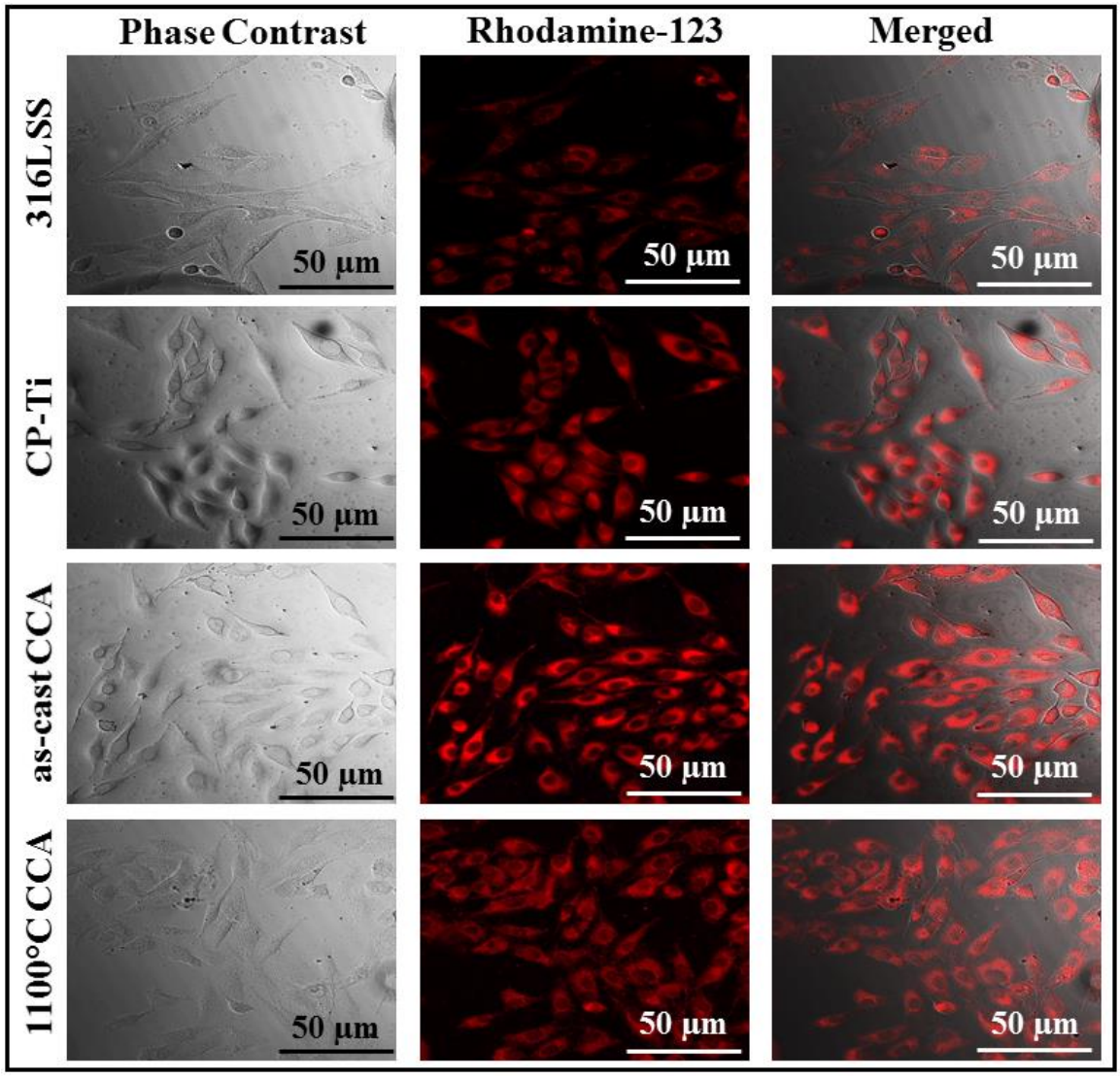

Figure 6.10 Confocal-fluorescence images of MG-63 cells stained with Rhodamine-123 (Rh-123, Mitochondria probe) on the surface of as-cast and 1100˚C annealed CCA, cp-Ti, and 316L SS.

The overall effectiveness of implant biomaterials depends not only on achieving the favorable cellular response at the interface between the implant and host tissue but also on the successful integration of the implant with the surrounding tissue. In MG-63 cells, processes such as angiogenesis, cell survival, proliferation, and energy metabolism are all associated with increased production of reactive oxygen species (ROS) [216].

In order to evaluate the impact of the as-cast and 1100 °C annealed CCA on ROS generation in MG-63 cells after three days of treatment, DCFH-DA staining was conducted, and the results are presented in Figure 6.11. Cells treated with both CCA conditions exhibited minimal green fluorescence, indicating low ROS production. In contrast, cells treated with 316L SS and CP-Ti showed significantly higher green fluorescence from 2,7-dichlorofluorescein, suggesting elevated ROS levels. Previous research reported that excessive ROS can promote apoptosis and hinder critical biological processes such as bone regeneration, fracture healing, and osseointegration of implant materials [216-217]. These observations suggest that the $Ti_{35}Zr_{35}Nb_{15}Mo_5Fe_5Cr_5$ CCA exhibits superior cytocompatibility compared to 316L SS and cp-Ti.

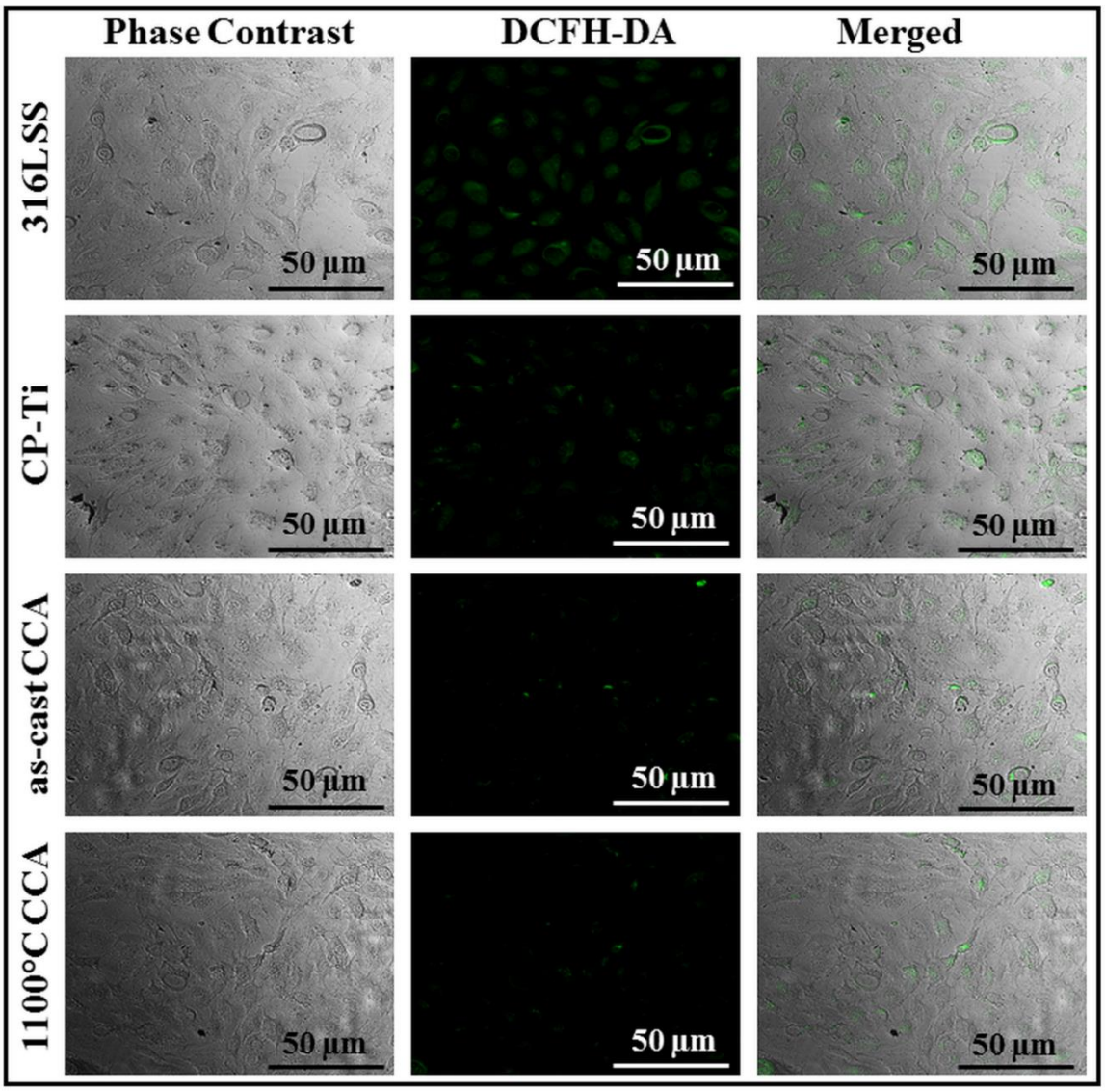

Figure 6.11 Intracellular reactive oxygen species generation in MG-63 cells after 3 days of treatment on the surface of as-cast and 1100˚C annealed CCA, cp-Ti, and 316L SS, visualized using DCFH-DA staining under confocal microscopy.

6.3 Discussion

The results presented in the previous section demonstrate that the $Ti_{35}Zr_{35}Nb_{15}Mo_5Fe_5Cr_5$ CCA exhibits excellent corrosion resistance and good biocompatibility compared to conventional implant materials such as 316L SS and cp-Ti. In light of these findings, a more detailed discussion is needed to explore the underlying factors

contributing to this exceptional combination of properties and to comprehensively assess the alloy's potential as an implant biomaterial.

6.3.1 Corrosion resistance of $Ti_{35}Zr_{35}Nb_{15}Mo_5Fe_5Cr_5$ CCA

Corrosion-induced degradation remains a major concern for metallic biomaterials, primarily due to the release of metal ions after the breakdown of the protective passive oxide layer. The deterioration of this layer often initiates localized corrosion phenomena, such as pitting, which act as sources for the continuous release of metal ions into the surrounding environment. To address these challenges, the design and development of corrosion-resistant alloys are essential, with the objective of minimizing ion release and preventing the formation of harmful corrosion by-products that could trigger adverse biological reactions. As presented in Table 6.1, the $Ti_{35}Zr_{35}Nb_{15}Mo_5Fe_5Cr_5$ CCA exhibits an exceptionally low corrosion current density (dissolution rate), ranging from 0.20 to 0.79 μA/cm². This dissolution rate is more than an order of magnitude lower than that of 316L stainless steel. Additionally, when compared to Ti-6Al-4V, which has a reported corrosion current density of 45 μA/cm² [218], the present CCA demonstrates a significantly reduced rate of metal ion release. These results demonstrate the alloy's outstanding corrosion resistance and its potential suitability for biomedical applications.

The excellent corrosion resistance of the $Ti_{35}Zr_{35}Nb_{15}Mo_5Fe_5Cr_5$ CCA in a simulated physiological environment can be attributed to the formation of a stable and protective passive oxide layer, promoted by its constituent elements. According to Wang et al. [67], Nb plays a key role in enhancing the thickness of this passive film, thereby improving corrosion resistance with increasing Nb content. A few studies reported the formation of stable oxides,

such as Cr_2O_3, TiO_2, ZrO_2, MoO_3, Nb_2O_5, and Fe_2O_3, on similar CCAs under physiological conditions [67,69,121]. The composition of this passive layer is influenced by the chemical activity and standard electrode potentials of the individual elements, with more chemically active elements or those with lower standard electrode potentials showing a greater affinity for oxygen and a stronger tendency to form oxides.

6.3.2 In-vitro biocompatibility of $Ti_{35}Zr_{35}Nb_{15}Mo_5Fe_5Cr_5$ CCA

The in-vitro biocompatibility assessment of both the as-cast and 1100°C annealed $Ti_{35}Zr_{35}Nb_{15}Mo_5Fe_5Cr_5$ CCA, carried out using MG-63 and HEK-293 cell lines, reveals enhanced cell viability, proliferation, and adhesion in comparison to 316L SS and cp-Ti. Previous studies have shown that cell adhesion and proliferation on biomedical materials are primarily influenced by surface characteristics, including topography or roughness, surface energy, and wettability (as indicated by contact angle measurements) [142-143,217,219]. Hydrophilic surfaces, characterized by contact angles less than 90°, typically promote cell adhesion by supporting the adsorption of proteins from the surrounding medium onto the material's surface. This protein layer creates a favorable environment for subsequent cell attachment [220-221]. Additionally, such surfaces usually possess higher surface free energy and lower contact angles, both of which contribute to improved interactions between cells and the implant surface.

Surface free energy is an intrinsic characteristic of solid materials that cannot be measured directly; however, it can be determined using contact angle measurements. The surface free energy, or the work of adhesion (W_{adh}), can be determined using the following equation [142].

$$W_{adh} = \gamma \times (1 + \cos\theta) \text{ ..... (6.2)}$$

where γ denotes the surface tension, and θ represents the contact angle. Surfaces with higher surface free energy have been shown to stimulate the production of pro-angiogenic growth factors and support the differentiation of human aortic endothelial cells. This indicates that such surfaces may enhance the biocompatibility of implant materials by promoting vascularization and improving tissue integration. Notably, surface free energy also plays a role in bacterial adhesion [143], with higher surface free energy generally associated with reduced bacterial attachment, thereby improving the suitability of these materials for biomedical applications.

The biocompatibility of the $Ti_{35}Zr_{35}Nb_{15}Mo_5Fe_5Cr_5$ CCA is closely related to its excellent corrosion resistance, which minimizes the release of metal ions into the surrounding physiological environment. Also, its high biocompatibility is attributed to the spontaneous formation of a cytocompatible surface oxide layer, which supports cellular adhesion and proliferation [40,68, 222-223]. As a result, the alloy remains chemically stable in biological conditions and does not leach harmful ions, thereby preserving its biocompatibility and improving its potential for use in biomedical applications.

6.4 Summary

In this chapter, the corrosion behaviour and in-vitro biocompatibility of the newly developed $Ti_{35}Zr_{35}Nb_{15}Mo_5Fe_5Cr_5$ bio-CCA were comprehensively investigated. The salient observations of this study are summarized below.

i. The corrosion resistance of both the as-cast and annealed $Ti_{35}Zr_{35}Nb_{15}Mo_5Fe_5Cr_5$ bio-CCA was superior to that of conventional implant biomaterials such as 316L SS and cp-Ti. In addition, corrosion resistance improved further with increasing annealing temperature, attributed to enhanced microstructural homogeneity resulting from the annealing treatment.

ii. SEM analysis of the corroded surfaces revealed that the as-cast CCA showed a small number of corrosion pits, whereas the alloy annealed at 1100°C exhibited an almost pit-free surface. This suggests that annealing at 1100°C promotes the creation of a highly stable passive film, which effectively reduces the release of metallic ions.

iii. In-vitro cell culture studies, including MTT assay, AO/EtBr staining, DAPI staining, Rh-123 staining, and DCFH-DA staining, showed that both the as-cast and 1100 °C annealed CCAs exhibited superior cell adhesion and proliferation, along with high cell viability, as compared to 316L SS and cp-Ti. These results demonstrate the alloy's promising potential for biomedical applications.